Disk Resonator Gyroscope with Whole-Angle Mode Operation

Parsa Taheri-Tehrani[1], Oleg Izyumin[2], Igor Izyumin[2], Chae H. Ahn[3], Eldwin J. Ng[3], Vu A. Hong[3], Yushi Yang[3], Thomas W. Kenny[3], Bernhard E. Boser[2], and David A. Horsley[1]

Email: {ptaheri}@ucdavis.edu {dahorsley}@ucdavis.edu

[1]University of California, Davis, CA, USA and [2]University of California, Berkeley, CA, USA and [3]Stanford University, Stanford, CA, USA

***Abstract*— We present a demonstration of a whole-angle mode operation of a 0.6 mm single-crystal silicon disk resonator gyroscope (DRG). This device has a Q factor of ~80,000 and a resonant frequency of ~250 kHz and is fabricated in the epi-seal process. Discrete-time control algorithms for rate-integrating gyro operation were implemented based on Lynch's algorithm. Despite the fact that this DRG is over 5 orders of magnitude smaller than the 58 mm HRG, the device's error sources are shown to be accurately modeled by the basic error models developed by Lynch.**

Keywords—MEMS; Gyroscope; Rate integrating; Whole angle mode; Discrete-time control; Disk resonator; Quadrature

I. INTRODUCTION

MEMS vibratory gyroscopes are based on small resonators that have at least two resonant modes that can be coupled by Coriolis force. There are two operational modes for a MEMS gyroscope: 1 – rate gyroscope (RG) mode in which angular rate is measured, and 2 – rate integrating gyroscope (RIG) mode in which the gyroscope measures the change in angle. In RG mode, the resonator is forced to oscillate at one of the resonant modes, and Coriolis force arising from rotation rate causes vibration in the second vibration mode; by sensing the vibration in this second mode, the applied rate can be measured. On the other hand, in RIG mode the gyro's vibration is not constrained to a fixed axis, and the Coriolis force causes the axis of vibration to freely precess, so that the precession angle of the oscillation provides a direct read-out of rotation angle. In an ideal, rigid-body resonator like a Foucault pendulum, the vibration direction tends to be constant relative to the global coordinate system and changes in the non-inertial frame (sensor frame). This provides a tool to measure the change in angle in the non-inertial frame. In flexural resonators, the vibration pattern's angle will change by a factor (<1) known as angular gain (AG) that dictates the scale factor for the RIG and is solely dependent on the geometry of the resonator and the vibration mode shape. Three major benefits of the RIG versus the RG are: 1 – direct angle measurement eliminates the error due to electronic integration of the RG output to calculate angle; 2 – stable scale factor as the scale factor (AG) is not affected by environmental variables such as pressure, voltage, and temperature; 3 – unlimited mechanical bandwidth (BW) in RIG. The RG's BW is limited by the resonator's quality factor when operated in an open-loop mode-matched condition [1, 2].

This work was funded by the DARPA micro-PNT program under contracts W31P4Q-11-1-0003 and N66001-12-1-4260, Program Manager Robert Lutwak.

In this paper we have implemented and studied the equations and control algorithms presented in Lynch [3] on a Disk Resonator Gyroscope (DRG). The effect of anisodamping error is also characterized by several measurements. The control algorithms are implemented on an FPGA with integrated soft processor. The performance of the gyroscope and error sources are studied for rate-integrating and force-to-rebalance modes. In [4, 5] similar approaches have been pursued to implement an RIG respectively on a bird-bath resonator with an angular gain of 0.25 and a quadruple mass gyroscope.

II. DEVICE AND TESTING PLATFORM

A. Device

The device, shown in Fig. 1(a) and first presented at MEMS 2013 [1] is a 0.6 mm single-crystal silicon disk resonator surrounded by 16 electrodes and fabricated in the epi-seal process. The device is operated in the 2θ vibration mode as illustrated in Figure 1(b). The angular gain between the two degenerate 2θ vibration modes is theoretically 0.8. This device has a *Q* factor of ~80,000 and a resonant frequency of ~250 kHz, corresponding to modal mass of 3.8 μg, and modal stiffness of 9500 N/m. The 16-electrode design of this resonator enables single-ended drive and differential sense and has electrodes for direct (frequency) tuning of both modes as well as cross-axis stiffness tuning for quadrature null.

B. Testing Platform

A stand-alone electronic platform consisting of a motherboard and daughterboard was designed to test the device. The daughterboard contains the gyro and analog front-end amplifiers for two differential sense channels and two single-ended drive channels along with five quasi-DC channels for bias and tuning voltages. The motherboard contains DACs

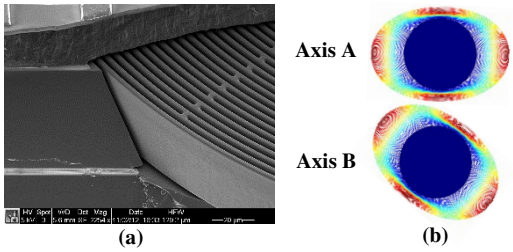

Fig. 1: (a) SEM image of the disk resonator (b) 2θ-mode shapes of the disk resonator.

and ADCs with 2 MHz sampling rate and an FPGA with integrated soft processor for digital signal processing. High-sample rate (2 MHz) operations including Phase-Locked-Loop (PLL), demodulation and modulation are implemented in hardware on the FPGA. Low sample-rate (2 kHz) discrete-time controllers are implemented on the soft processor, and registers are used to receive and send data through USB to and from a PC. The PCB is mounted on a rate-table, with electric power supplied using rate-table slip rings; a wireless USB connection allows unrestrained rotation.

III. Control Algorithm

MEMS resonators are not ideal; in particular, the damping and stiffness coefficients are different for each mode, and also there are damping and stiffness coupling terms between the two modes. These main sources of error in gyroscopes are known respectively as anisodamping and anisoelasticity. The difference in stiffness between resonant modes and the stiffness coupling between them, which produces quadrature error, can be compensated by electrostatic tuning using appropriately designed electrodes [1, 2, 6, 7].

Following electrostatic tuning, two closed-loop controllers are used to enable RIG mode operation. First, closed-loop energy control is implemented to maintain the vibration amplitude of the resonator without constraining the axis of vibration. Then, the residual anisoelasticity error remaining after electrostatic tuning is compensated using a closed-loop quadrature controller.

A third controller can be enabled which maintains the vibration angle at a fixed set-point, causing the gyroscope to operate as an RG in force-to-rebalance mode. The benefit of this mode is the high BW of the sensor, which will be determined by the BW of the closed-loop system defined by appropriate design of the PI controller. This controller is not used during RIG mode operation but allows the vibration angle to be set arbitrarily in order to characterize angle-dependent bias and quadrature terms that impact RIG performance.

Energy and quadrature variables as described in [3] are formulized in eq. (1) along with variables R and S:

$$\begin{cases} E = {x_s}^2 + {x_c}^2 + {y_s}^2 + {y_c}^2 \\ Q = 2(x_c y_s - y_c x_s) \\ R = {x_s}^2 + {x_c}^2 - {y_s}^2 - {y_c}^2 = \sqrt{E^2 - Q^2}\cos 2\theta \\ S = 2(x_c y_c - y_s x_s) = \sqrt{E^2 - Q^2}\sin 2\theta \end{cases} \quad (1)$$

In these equations: x_c and x_s are in-phase and quadrature signals from axis A, and y_c and y_s are in-phase and quadrature signals from axis B, θ is the precession angle, E is the vibration energy, Q is the quadrature, while R and S are variables used to calculate the precession angle such that: $\theta = 0.5\,tan^{-1}(S/R)$.

Fig. 2 shows the detailed block diagram of the control systems implemented. One PI controller, with output F_Q, is used to null Q, and a second PI controller, with output F_E, is used to the regulate the value of E to E_0. Having Q eliminated and E controlled, the value of S dictates the angle of vibration, so a third PI controller is used to control S. More detailed analysis is presented in following subsections.

A. Open-loop Electrostatic Tuning

Frequency mismatch $\Delta\omega$ between the two modes results from the anisotropic stiffness of <100> single-crystal Si, which is compensated by the DRG design [6]. The residual $\Delta\omega$ is reduced from 1382 rad/s to 6.3 rad/s through an initial open-loop tuning procedure using electrostatic tuning electrodes. A similar procedure is used to null the initial quadrature error to a value of 31 dps from the 319 dps as-fabricated value.

B. Quadrature Control

The quadrature control loop operates according to eq. (2):

$$\dot{Q} \approx -\frac{2}{\tau}Q - \Delta\omega sin2(\theta - \theta_\omega)E + \frac{\sqrt{E}}{\omega}F_Q \quad (2)$$

where $1/\tau$ is the average of the inverse of the time constant of the two modes, θ_ω is the primary axis of stiffness associated with anisoelasticity, $\Delta\omega$ and ω are respectively associated with the difference and the average of the resonant frequencies of the two modes, and F_Q is the force magnitude of the quadrature

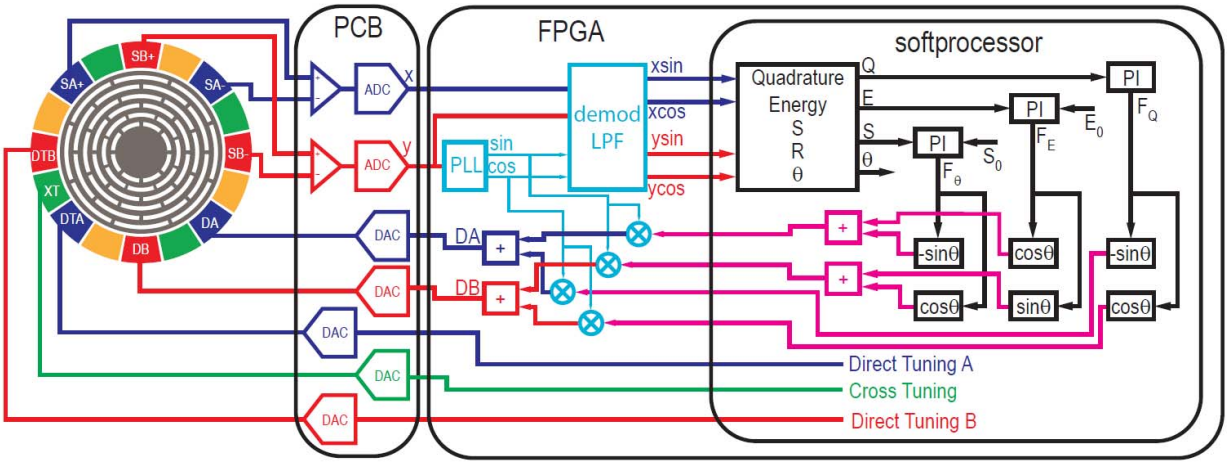

Fig. 2: Block diagram of the electronics and the control loops, including three closed loop controller for Quadrature Cancellation, Energy stabilization, and angle control for force-to-rebalance mode. The DC voltages to apply tuning voltages are also adjusted in the soft processor

PI controller.

C. Energy Control

The energy control loop operates according to eq. (3):

$$\dot{E} \approx -\left[\frac{2}{\tau} + \Delta\left(\frac{1}{\tau}\right) cos2(\theta - \theta_\tau)\right] E - \frac{\sqrt{E}}{\omega} F_E \quad (3)$$

where $\Delta(1/\tau)$ is the difference of the inverse of the time constant of the two modes, θ_τ is the primary axis of damping associated with anisodamping, and F_E is the output of the energy PI controller.

D. Angle Control

The angle control loop operates according to eq. (4):

$$\dot{\theta} \approx -AG \cdot \Omega + \frac{1}{2}\Delta\left(\frac{1}{\tau}\right) \sin 2(\theta - \theta_\tau) + \frac{1}{2}\Delta\omega cos2(\theta - \theta_\omega)\frac{Q}{E} - \frac{F_\theta}{2\omega\sqrt{E}} \quad (4)$$

where AG is angular gain, Ω input rate, and F_θ is the output of the angle PI controller.

E. Control Forces

As shown in Fig. 2, the control forces are not applied directly to the gyro, but are instead applied to the two separate axes as illustrated in Fig. 2 and eq. (5):

$$\begin{cases} F_{Y_s} = F_E \sin\theta + F_\theta \cos\theta \\ F_{X_s} = F_E \cos\theta - F_\theta \sin\theta \\ F_{Y_s} = F_Q \cos\theta \\ F_{X_s} = -F_Q \sin\theta \end{cases} \quad (5)$$

IV. Experimental Results

A. Quadrature and Energy Control

To measure the DRG's angle-dependent quadrature error, the angle set-point was varied over 360° and the energy, E, and the output of the quadrature null controller, F_Q, were measured, Fig. 3. The observed quadrature follows the expected sin2θ dependence described in eq. (2). The maximum value of quadrature, 33.3 dps, is calculated using the scale factor measured from force-to-rebalance mode operation presented later in the paper. The quadrature controller is able to suppress the ratio of quadrature to vibration energy (Q/E) from an initial value of 86% to 0.1%.

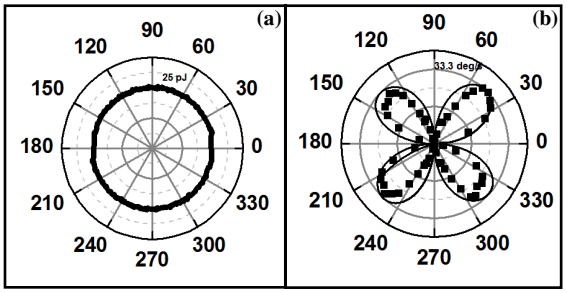

Fig. 3: (a) Measured energy versus set-point angle (b) Measured (points) and simulated (line) quadrature nulling force versus set-point angle.

B. Anisodamping Error

The error originating from anisodamping was studied experimentally. First, the quality factor of the two resonant modes was measured using frequency response measurements to be 80,807 and 78,282, which results in $\Delta(1/\tau)$ = 0.32 Hz.

Assuming quadrature is nulled (Q = 0), no control force is applied to set the angle (F_θ = 0), and no rate is applied (Ω = 0) eq. (4) is reduced to:

$$\dot{\theta} \approx \frac{1}{2}\Delta\left(\frac{1}{\tau}\right) \sin 2(\theta - \theta_\tau) \quad (6)$$

This equation explains the rotation of θ towards the primary axis of damping with a sin2θ-dependent anisodamping term. This equation produces an accurate fit to the experimental results. The effect of anisodamping was characterized by releasing the angle from an initial set point and observing the exponential decay time-constant, $\Delta(1/\tau)$ = 0.3 Hz, Fig. 5(a). Including rate input, the linearized form of eq. (4) for small changes of θ can be rewritten in the frequency domain:

$$\frac{\theta_o}{\theta_i} = \frac{-AG \times j\omega}{j\omega - \Delta\left(\frac{1}{\tau}\right)} \quad (7)$$

eq. (7) shows that the RIG including anisodamping will behave like a high pass filter with a cut-off frequency of $\Delta(1/\tau)$. To investigate this behavior, sinusoidal rotations with an amplitude of 6° with different frequencies were applied to the gyroscope. The ratio of the sensor's output, θ_o, and the 6° input, θ_i, versus frequency is plotted in Fig. 5(b). Fitting the experimental data with eq. (7) results in $\Delta(1/\tau)$ = 0.3 Hz, equal to the two earlier measurements. Also the angular gain can be calculated from the amplitude of the flat region (-2.14 dB) which corresponds to a value of 0.78, in good agreement with the theoretical value.

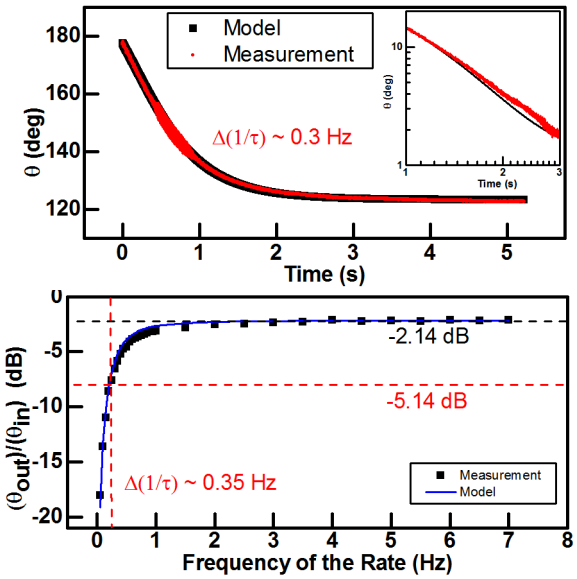

Fig. 4: (a) The decay of the angle toward the primary axis of damping (θ_τ = 123°) with decay time constant $\Delta(1/\tau)$ = 0.3 Hz. (b) Swept frequency rate measurements confirm $\Delta(1/\tau)$ = 0.3 Hz. The measured angular gain is 0.78 (= -2.14 dB).

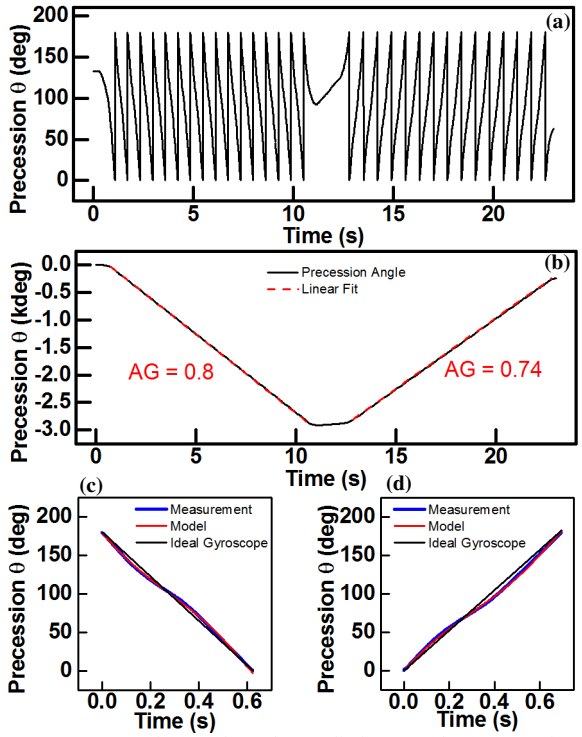

Fig. 5: Gyro precession angle under applied CW and CCW rotations of 3600 deg with 360 dps rate (a). Unwrapped precession angle for same test (b). Close-up of CW (c) and CCW (d) rotation inputs. The deviation from ideal behavior (black lines) matches the sinusoidal $\Delta(1/\tau)$ error predicted by Lynch's model (red lines).

C. Rate Test

Rate tests were performed on the gyroscope to analyze the performance and also to characterize the anisodamping error source. Looking at eq. (8), which includes the rate input:

$$\dot{\theta} \approx -AG \cdot \Omega + \frac{1}{2}\Delta\left(\frac{1}{\tau}\right)\sin 2(\theta - \theta_\tau) \quad (8)$$

Angular gain and $\Delta(1/\tau)$ are values that can be extracted by fitting the rate test results with this equation. Fig. 5 shows the plots from rate tests. A rotation of 3600 deg with constant speed of 360 dps was applied to the gyroscope in both directions. Fig. 5(a) shows the precession angle of the RIG. The unwrapped precession angle is plotted in Fig. 5(b) to analyze the overall angular gain of the RIG, resulting in an AG of 0.8 and 0.74. A closer look at the rate data is presented in Fig. 5 (c,d) where eq. (8) is fit to the measured data. The AG values calculated are 0.8 and 0.73, respectively, comparable to values calculated from Fig. 5(b). The $\Delta(1/\tau)$ values calculated are 0.36 Hz and 0.33 Hz, respectively, equal to values presented earlier in the paper.

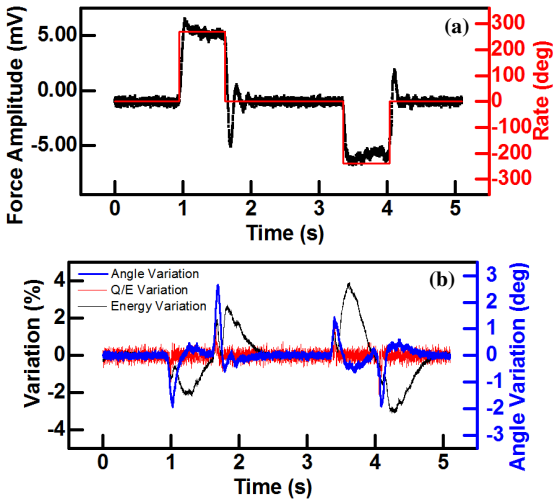

Fig. 6: Force-to-rebalance rate-gyro operation. (a) Rebalance force in response to rate step inputs corresponds to 21 μV/(deg/s) scale factor. (b) Transient response of controlled variables shows tracking error exhibited during rate transients. Energy is constant within 4%, Q/E within 1%, and angle error is less than 3°.

D. Force-to-Rebalance Mode

Operation in force-to-rebalance RG mode was implemented on the same device by activating the angle control loop and applying a trapezoidal input profile (Ω_1 = 240 dps, Ω_2 = 0 dps, Ω_3 = -270 dps). The effort to keep the vibration angle constant is plotted in Fig. 6(a), corresponding to a scale factor of 21 μV/deg/s. The transient behavior of the controlled variables (E, Q, and θ) in response to rate inputs is shown in Fig. 6(b) and demonstrates that the transient amplitudes are small.

V. Summary

We have presented an implementation of Lynch's equations on a disk resonator gyroscope on a standalone control system. Despite the DRG's low time constant of 100 ms, the gyroscope is successfully operated as a RIG. Through various experiments, we show that the DRG's error sources are well-described by Lynch's error model. Understanding the error originating from anisodamping is the first step in characterizing the resonator to allow implementing more advanced control systems to compensate this error in the RIG.

References

[1] S. Nitzan, C.H. Ahn, T.-H. Su, M. Li, E.J. Ng, S. Wang, Z.M. Yang, G. O'Brien, B.E. Boser, T.W. Kenny, D.A. Horsley, "Epitaxially-encapsulated polysilicon disk resonator gyroscope," *IEEE Micro Electro Mechanical Systems (MEMS), 26th International Conference*, pp.625-628, 20-24 Jan. 2013

[2] T.-H. Su, S. Nitzan, P. Taheri-Tehrani, M.H. Kline, B.E. Boser, D.A. Horsley, "Silicon MEMS Disk Resonator Gyroscope With an Integrated CMOS Analog Front-End," *IEEE Sensors Journal*, vol.14, no.10, pp.3426-32, Oct. 2014.

[3] D. D. Lynch, "Vibratory Gyro Analysis by the Method of Averaging" *Proc. 2nd Saint Petersburg Int. Conf. on Gyroscopic Technology and Navigation*, pp. 26-34, May 1995.

[4] J.-K. Woo, J.Y. Cho, C. Boyd, K. Najafi, "Whole-angle-mode micromachined fused-silica birdbath resonator gyroscope (WA-BRG)," *IEEE Micro Electro Mechanical Systems (MEMS), 27th International Conference*, pp. 20-23, 26-30 Jan. 2014

[5] A.A. Trusov, D.M. Rozelle, G. Atikyan, S.A. Zotov, B.R. Simon, A.M. Shkel, A.D. Meyer," Non-Axisymetric Coriolis Vibratory Gyroscope with Whole Angle, Force Rebalance, And Self-Calibration", *Solid-State Sensors, Actuators and Microsystems Workshop*, Hilton Head Island, South Carolina, June 8-12, 2014

[6] C.H. Ahn, E.J. Ng, V.A. Hong, Y. Yang, B.J. Lee, I. Flader, T.W. Kenny, "Mode-Matching of Wineglass Mode Disk Resonator Gyroscope in (100) Single Crystal Silicon," *Journal of Microelectromechanical Systems,* , to be published.

[7] S. Sonmezoglu, S.E. Alper, T. Akin, "An Automatically Mode-Matched MEMS Gyroscope With Wide and Tunable Bandwidth," *Journal Microelectromechanical Systems,* vol.23, no.2, pp.284-97, April 2014.